HHS Public Access

Author manuscript

Magn Reson Med. Author manuscript; available in PMC 2019 May 01.

Published in final edited form as:

Magn Reson Med. 2018 May ; 79(5): 2724–2730. doi:10.1002/mrm.26895.

Chemical shift encoding (CSE) for sensitive fluorine-19 MRI of perfluorocarbons with complex spectra

Ruud B van Heeswijk[1,*], **Roberto Colotti**[1], **Emeline Darçot**[1], **Jean Delacoste**[1], **Maxime Pellegrin**[2], **Davide Piccini**[1,3], and **Diego Hernando**[4,5]

[1]Department of Radiology, University Hospital (CHUV) and University of Lausanne (UNIL), Lausanne, Switzerland [2]Division of Angiology, Heart and Vessel Department, Lausanne University Hospital (CHUV), Lausanne, Switzerland [3]Advanced Clinical Imaging Technology, Siemens Healthcare AG, Lausanne, Switzerland [4]Department of Radiology, University of Wisconsin-Madison, Madison WI, USA [5]Department of Medical Physics, University of Wisconsin-Madison, Madison WI, USA

Abstract

Purpose—To implement a fluorine-19 (^{19}F) chemical shift encoding (CSE) approach for the sensitive imaging of molecules with multi-resonance spectra in order to remove their chemical shift displacement (CSD) artifacts, and to characterize its sensitivity versus established pulse sequences.

Methods—The feasibility of CSE spoiled gradient echo (GRE) and balanced steady-state free precession (bSSFP) was first demonstrated in a phantom study. The dependence of the sensitivity of CSE-bSSFP on several pulse sequence parameters was then established, after which the occurrence of out-of-plane excitation was assessed for 2D and 3D techniques. Next, the sensitivity (in $mm^{-3}s^{-0.5}$) of both CSE techniques was compared to bSSFP ultrashort-echo-time (bSSFP-UTE) imaging and multi-chemical-shift-selective turbo spin echo (MCSS-TSE) in a second phantom study. Finally, the sensitivity of the CSE-bSSFP, bSSFP-UTE and MCSS-TSE pulse sequences was compared in a preliminary in vivo mouse study.

Results—Both CSE approaches were successfully implemented and resulted in negligible residual CSD artifacts, while large-volume 3D acquisitions should be considered to reduce problems related to out-of-plane excitation. CSE-bSSFP was shown to have a higher sensitivity than the bSSFP-UTE and MCSS-TSE pulse sequences (15.8±1.3 vs. 11.7±1.0 vs. 13.3±0.9$mm^{-3}s^{-0.5}$, respectively, $P<0.001$), while the CSE-GRE technique had a lower sensitivity (4.8±1.1$mm^{-3}s^{-0.5}$).

Conclusion—CSE ^{19}F MR imaging enables the unambiguous visualization of compounds with complex spectra, and provides high sensitivity both in vitro and in vivo.

[*]Corresponding Author: Ruud B. van Heeswijk, PhD, Lausanne University Hospital (CHUV), RAD BH08.084, Rue du Bugnon 46, 1007 Lausanne, Switzerland, tel. +41-21-3147535, ruud.mri@gmail.com.

Introduction

Fluorine-19 (^{19}F) MR imaging of perfluorocarbons emulsions (PFCs) is increasingly used for cell tracking and inflammation imaging in preclinical research (1,2). Since fluorine has a very low natural abundance in the body, ^{19}F MRI enables direct and highly specific visualization of the PFC distribution. PFCs are furthermore biologically inert and are cleared from the tissue when their carrier cells die, which allows ^{19}F MRI to be used for cell tracking and monitoring over time (3). This technique has for example been used to track specific in-vitro-labeled immune cells (4,5) and stem cells (6,7), while it has also been used to image non-specific immune cell recruitment in animal models of such diseases as myocardial infarction (8), arthritis (9), myocarditis (10), and inflammatory bowel disease (11).

Several clinical trials that use ^{19}F MRI to track cell populations in patients have recently also been initiated (12). One of the most significant challenges for the initiation of such clinical trials is the requirement that PFCs have to have been proven to be safe and biocompatible. Several perfluorocarbons, such as perfluorooctyl bromide (PFOB) and perfluorodecalin, already passed such trials as oxygen carriers and blood volume expanders (13), and their use would thus encounter fewer hurdles for ^{19}F MR-driven trials. Unfortunately, the PFCs with the most promising biocompatibility profile (14), i.e. the ones that are retained for the shortest time in the liver and spleen such as PFOB, have complex MR spectra with multiple resonances. These resonances are often spread over a broad frequency range (up to 10,000Hz at 3T) and create chemical shift displacement (CSD) artifacts that “dilute” the signal over multiple voxels. This decreases the already low signal-to-noise ratio (SNR) and confounds image interpretation. In order to address this challenge, several techniques have been described for the removal of CSD artifacts in ^{19}F MRI. Most of these techniques are based on spectroscopic imaging (15), which is slow since it needs to encode an extra dimension, a deconvolution filter in the image domain (16,17) that forces a regularization that can remove fine details, spectrally selective excitation (18-20) that does not exploit all ^{19}F atoms to generate the signal, or a combination of these (21).

Instead of attempting to suppress the additional resonances or to selectively excite a subset of resonances, we propose a multi-echo chemical shift-encoded (CSE) approach that combines a multi-echo acquisition with prior-knowledge-constrained image reconstruction. CSE can in principle be used with any pulse sequence in which the echo time TE can be varied in small increments (on the order of 0.05-0.5ms) in a series of acquisitions.

Therefore, the overall goal of this work was to develop and evaluate a CSE approach for ^{19}F MRI of PFCs with complex spectra. This development was performed in two steps. 1) As a proof-of-concept, we implemented the CSE approach with spoiled gradient echo (GRE) imaging. CSE-GRE is relatively simple to implement and model, and enables assessment of image quality and sensitivity. However, GRE acquisitions typically have relatively low SNR efficiency; an implementation of CSE with higher-SNR pulse sequences is therefore highly desirable. 2) For these reasons, we extended the proposed CSE technique to balanced steady-state free precession (bSSFP) imaging. Due to the off-resonance signal modulation of bSSFP pulse sequences, CSE-bSSFP requires more careful signal modeling than CSE-GRE.

However, CSE-bSSFP may provide substantial improvements in SNR and sensitivity, as well as broader applicability. Finally, in this study we aimed to characterize the sensitivity of CSE-GRE and CSE-bSSFP relative to several other recently reported sensitive ^{19}F MRI techniques.

Theory

We here describe the proposed reconstruction for a CSE acquisition in the presence of multiple ^{19}F resonances with different frequency shifts f_m. Unlike in common ^{1}H MRI applications, the large frequency shifts f_m observed in ^{19}F MRI can result in substantial CSD (and therefore image degradation) even in Cartesian acquisitions with high receiver bandwidth. To avoid these CSD artifacts, the reconstruction can be formulated as a direct least-squares fit in k-space. Assuming prior knowledge about the spectral and relaxation properties of the compound of interest, the parameter map estimate $\rho(x, y)$ that best fits the acquired k-space data $s_{TE}(k_x, k_y(t), t)$ can be reconstructed(22). The k-space signal obtained with a CSE 2D Cartesian pulse sequence can be modeled as:

$$s_{\mathrm{TE}}(k_x, k_y(t), t) = \iint_{x,y} \rho(x,y)\left[\sum_{m=1}^{M} A_m \exp(i2\pi\cdot(\mathrm{TE}+t)f_m)\, C_m\right]\exp(i2\pi x k_x)\exp(i2\pi y k_y(t))\,\mathrm{dxdy}, \quad (1)$$

where x and y are the phase-encoding and readout directions respectively, TE is the echo time, t is the time relative to the center of the current readout (i.e. relative to TE), ρ is the overall signal amplitude composed of M resonances with relative amplitudes A_m and chemical shifts f_m (in this study, M=1-7 was used), while C_m describes additional known pulse-sequence-specific signal modulations. When a GRE pulse sequence is used, C_m can be well modeled as:

$$C_m = \mathrm{B}_m \cdot \exp(-(\mathrm{TE}+t)/T_2^*), \quad (2)$$

where B_m is the relative radiofrequency (RF) pulse amplitude at chemical shift f_m. No RF phase modulation is assumed here, but this could be easily added if needed. When a bSSFP pulse sequence is used, C_m can be calculated for each time point $TE + t$ and chemical shift f_m through Bloch equation simulations, for which the RF excitation angle α, the T1 and T2 relaxation times, and the repetition time TR are used as input. In this work, the reconstruction is formulated as a linear least-squares fitting problem using Eq. 1 as the signal model. Because the phase-encoding direction is not affected by CSD artifacts, the reconstruction can be solved separately for each location x.

Methods

Implementation

All experiments were performed on a 3T clinical MR scanner (Magnetom Prisma, Siemens Healthcare, Erlangen, Germany) with a 35-mm-diameter transmit/receive birdcage RF coil (Rapid Biomedical, Rimpar, Germany) that is tunable to both the ^{19}F and ^{1}H frequencies. A PFOB emulsion was prepared as described previously (14) at a ^{19}F concentration of 23.85M (i.e. a PFOB concentration of 1.40M). A phantom was constructed from five 1ml syringes filled with PFOB that was diluted 4, 8, 16, and 32 times in 2%w/v agar (Sigma-Aldrich, St. Louis, MO, USA). The last syringe contained only 2%w/v agar and no PFOB. These syringes were then placed in a plastic 50ml centrifuge tube with 2%w/v agar.

We implemented a prototype two-dimensional (2D) CSE GRE pulse sequence to acquire 7 images with TEs from 3.28 to 3.88ms and increment ΔTE=0.1ms (one echo acquired per TR), TR=8.1ms, acquisition bandwidth BW=300Hz/pixel, α=8°, matrix size 256×256, voxel size V=0.5×0.×5×2mm^3, 64 averages and total scan time T_{acq}=15min29s. A similar three-dimensional (3D) version with matrix size 256×256×32, and 2 averages was also implemented to demonstrate the equivalence of the 3D application of CSE.

Based on the 2D and 3D CSE GRE versions, 2D and 3D CSE bSSFP acquisitions were implemented with TE=3.1-3.7ms, ΔTE=0.1ms, TR=6.7ms, α=60°, and a total scan time T_{acq}=12min15s. After ^{1}H scout scanning and shimming, the three pulse sequences were acquired centered on the same slice in the phantom. The relaxation times of the PFOB resonances were obtained from Colotti et al. (23). Image reconstruction from the k-space data was performed in Matlab (the MathWorks, Natick, MA, USA).

Pulse Sequence Characterization

Given that bSSFP is subject to off-resonance banding artifacts that vary with TR (24) and might thus suppress signal from some of the PFOB resonances, the influence of the TR (from 6 to 8ms as well as from 3 to 8ms with twice the sampling bandwidth) on the total signal was characterized through Bloch equation simulations. In order to normalize and compare the obtained signal at different TRs of the simulations, the sensitivity S was defined as the simulated signal divided by the square root of the TR.

In a second characterization study in the previously mentioned phantom, the influence of ΔTE on the sensitivity S in the bSSFP version of CSE was explored for a range of ΔTE from 0.05 to 0.5ms and for 1 to 5 echoes. In this phantom study, the sensitivity was defined as:

$$S=\mathrm{SNR}/(V\sqrt{T_{\mathrm{acq}}}). \quad (3)$$

Since a birdcage volume coil was used without any acceleration techniques, the SNR of a region of interest (ROI) was defined as the ratio of the average signal of the ROI divided by the standard deviation of the noise in an ROI in the background well outside any object.

In order to determine to what degree the different resonances cause signal from outside the intended slice to be excited, a 2D ^{19}F bSSFP image with the abovementioned parameters, the shortest TE, and a 5mm slice thickness was acquired in the PFOB phantom. The slice was placed through the syringe without PFOB and at 5mm distance from the other syringes, such that the image slice itself should contain no ^{19}F signal and to avoid excitation of the other syringes caused by a poor RF profile. To demonstrate the influence of the slice selection gradient on extent of the out-of-slice excitation, three different sinc RF pulses that require different slice selection gradients (9.2, 12.2, and 17.5mT/m) were then used to acquire the same slice. A 3D ^{19}F bSSFP version with 32 slices of 5mm thickness that easily covered the entire phantom was also acquired at the same position and with the fastest RF pulse.

Comparison of Sensitivity

The sensitivity of the abovementioned 2D and 3D CSE- GRE and bSSFP protocols was compared to two previously published sensitive multi-resonance imaging techniques at 3T in the PFOB phantom. The first was ultrashort-echo-time imaging with a bSSFP readout (bSSFP-UTE) and a phyllotaxis 3D radial trajectory (25), which has the advantage that it can be used to acquire all the CF_2 resonances before they dephase through J-coupling (19). The acquisition was performed with TE=90μs, TR=2.6ms, acquisition bandwidth BW=405Hz/pixel, α=30°, matrix size 128^3, V=1×1×1mm^3, 125,952 lines, no averaging, and T_{acq}=4min30s. The second technique was 3D multiple-chemical-shift-selective turbo spin echo (MCSS-TSE), which uses the waiting time of a 3D TSE sequence to selectively excite and image the different resonances, thus avoiding J-coupling in all except the central γ-$\delta\varepsilon$-ζ multiplet (20). The acquisition was performed with TE=13.7ms, echo train length 14, TR=1700ms, acquisition bandwidth BW=150Hz/pixel, a sinc RF pulse with an excitation bandwidth of 260Hz, matrix size 256×256×8, V=0.5×0.5×2mm^3, no averaging, and T_{acq}=5min21s.

The compared pulse sequences used a different readout bandwidth, which also has an influence on the SNR. However, all bandwidths were the lowest possible at the used resolutions, except in the case of the bSSFP-UTE, where an even lower bandwidth would have resulted in undesirable increases of TE.

In Vivo Validation

To demonstrate the sensitivity of CSE in vivo, the three most sensitive pulse sequences were repeated in mice. All animal experiments performed in this study were approved by the regional animal ethics committee. Four adult female apolipoprotein-E-knockout (apoE$^{-/-}$) mice (which express an elevated degree of inflammation (26)) were injected intraperitoneally with 300μl of PFOB. After a 24h waiting period to allow the PFOB to accumulate in the liver and spleen, anatomic ^{1}H MRI was performed in a sagittal orientation and centered on the liver, and was followed by localized shimming. ^{19}F MRI was performed centered on the same location with CSE-bSSFP, bSSFP-UTE, and MCSS-TSE, with the same pulse sequence parameters as described earlier.

Statistical analysis

The significance of all differences in sensitivity was tested with unpaired two-tailed Student's t-tests with Bonferroni correction for multiple comparisons where applicable, and with $P<0.05$ considered significant. Results are presented as mean ± standard deviation (SD).

Results

Pulse Sequence Characterization

CSE was successfully implemented for both GRE and bSSFP imaging of PFOB. The CSE-GRE technique reduced the CSD artifacts from all PFOB resonances to a degree where they were indistinguishable from the background noise. The CSE-bSSFP technique similarly eliminated the CSD artifact from the CF_2Br resonance, while ~4% of the CSD artifact from the CF_2 multiplet remained (Figure 1).

The numerical simulations of the influence of the TR on the sensitivity of CSE-bSSFP demonstrated that while there is a minor general decrease in sensitivity with the increase of TR (~5% over 2ms), there are also clear sensitivity minima where the bSSFP banding artifacts cancel out one or more resonances (Figure 2A). The phantom study on the influence of ΔTE on the sensitivity similarly demonstrated that after a broad optimal range, an increase in ΔTE (which increases TR) leads to a decrease in sensitivity (Figure 2B). At lower echo numbers and longer ΔTE there are furthermore more significant residual CSD artifacts.

An increasing amount of out-of-slice signal was excited with the 2D CSE-bSSFP technique with the decreasing slice-selection gradient strengths, while no signal was displaced into the equivalent slice within the 3D CSE-bSSFP technique (Figure 3).

Comparison of Sensitivity

The 3D versions of CSE-GRE and CSE-bSSFP resulted in the exact same sensitivities as their 2D counterparts. When reconstructing the MCSS-TSE images for the phantom sensitivity comparison, the γ-δε-ζ CF_2 resonances were consistently extremely blurred to the degree that individual syringes were no longer recognizable, and were thus not included in the summed image reconstruction. A minor overall blurring was also observed in the reconstructed bSSFP-UTE images. For the sake of clarity and since the results were highly similar in the other syringes, only the measurements in the syringe with the highest PFOB concentration results are reported here. The phantom comparison of the CSE techniques to bSSFP-UTE and MCSS-TSE pulse sequences resulted in a slightly higher sensitivity of the CSE-bSSFP technique than of the bSSFP-UTE and MCSS-TSE pulse sequences (15.8±1.3 vs. 11.7±1.0 vs. 13.3±0.9$mm^{-3}s^{-0.5}$, respectively, with $P<0.001$ for all comparisons), while the CSE-GRE technique had a lower sensitivity than the other techniques (4.8±1.1$mm^{-3}s^{-0.5}$, Figure 4).

In Vivo Validation

The animal studies resulted in broadly similar sensitivity differences as observed in phantoms (CSE-bSSFP: 2.56±0.66, bSSFP-UTE: 2.24±0.51, MCSS-TSE: $1.97\pm0.53 mm^{-3}s^{-0.5}$), although the differences between the techniques were smaller, and bSSFP-UTE outperformed MCSS-TSE. Further, there were minor residual CSD artifacts in the CSE-bSSFP images (Figure 5). However, no differences were statistically significant ($P>0.20$ for all, before Bonferroni correction).

Discussion

In this study, we successfully implemented a chemical shift encoding technique for imaging of perfluorocarbons with high sensitivity and free of CSD artifacts. The proposed technique may have important applications for cell tracking and inflammation imaging in preclinical research as well as in clinical applications, particularly in the presence of perfluorocarbons with complex MR spectra (such as PFOB).

CSE-GRE was demonstrated to be a relatively robust and simple implementation, but as is typical for GRE, it lacked sensitivity. This was addressed with CSE-bSSFP, which had substantially higher sensitivity and SNR, but required more complicated modeling, including off-resonance signal modulations inherent to bSSFP. This higher sensitivity of CSE-bSSFP at 3T will most likely be required in future patient applications, where only low concentrations of PFC are expected to accumulate in regions of interest. Such patient applications will most likely be carried out with more sensitive surface RF coils, whose distance-dependent RF transmission and sensitivity should not have an effect on the performance of the CSE approaches until the effective RF excitation angle decreases by an order of magnitude. In this case, the CSE approaches may thus offer superior depth penetration to TSE-based pulse sequences.

The numerical simulations of the dependence of the sensitivity of the proposed technique on the TR of CSE-bSSFP indicated that the TR should be carefully chosen in order to avoid a ~30% drop in sensitivity. In contrast, the phantom study on the influence of ΔTE demonstrated that ΔTE can be chosen over a fairly broad range of 0.1-0.3ms. Since an increase in ΔTE causes an increase in TR, there is most likely interplay between the two parameters that could be the cause of the lower sensitivity of the proposed technique at the lower ΔTE values, although the lower ΔTE values might also result in insufficient differences in phase evolution between the multi-echo images to properly encode the resonances. It should also be noted that acquiring multiple echoes directly after a single excitation could perhaps significantly decrease the acquisition time, but it would most likely also result in prohibitively long ΔTE and TR values, although this remains to be investigated.

The observed higher sensitivity at 3T of CSE-bSSFP compared to MCSS-TSE and bSSFP-UTE might be explained by several factors. While it is very fast, bSSFP-UTE uses a 3D radial readout and half-echoes, which both result in lower SNR. It furthermore selectively excites the CF_2 resonances, which means that only 12/17 ^{19}F atoms were used to generate a signal (19). Conversely, UTE imaging is also subject to a smoothing function due to the

influence of minute gradient imperfections during the start of the readout (27), which could result in an apparent increased SNR that does not reflect the true sensitivity of the pulse sequence. The MCSS-TSE pulse sequence most likely performs sub-optimally at 3T due to the challenge in balancing a short TE with long RF pulses that can separately excite the close γ-δε-ζ CF_2 resonances (23). With the RF pulses used in this study (as well as with 5ms sinc pulses that were not reported here), the γ and ζ resonances could not be excited separately from the δε resonance, which resulted in a very short apparent T_2 relaxation time that removed most signal and caused extensive blurring. Leaving the γ-δε-ζ resonance out of the reconstruction then resulted in only 9/17 ^{19}F atoms that contributed to the signal. In contrast, the CSE approach was applied to fast Cartesian imaging pulse sequences of all ^{19}F atoms in PFOB, which resulted in higher sensitivity. The lack of significance in the in vivo experiments is most likely caused by both inter-animal variability and the low sample number. The obtained phantom and in vivo sensitivity results are furthermore specific to the magnetic field strength and ^{19}F compound.

The presented CSE approach has several drawbacks. First, main magnetic field (B_0) and RF field (B_1) inhomogeneities were not measured or modeled in this implementation, which could cause inaccuracies in the proposed reconstruction, and thus residual CSD artifacts and a decreased sensitivity. This was likely the cause of the relative decrease in sensitivity of CSE-bSSFP in vivo. However, both B_0 and B_1 maps could be obtained through ^1H imaging, and included in the proposed algorithm in a fairly straightforward manner. Second, related to this, because of the possibility of dark band artifacts in bSSFP imaging, ^{19}F signal from the central resonance might be cancelled out near regions of interest at higher magnetic field strengths, which might be countered by lowering the TR through increasing the sampling bandwidth at the cost of sensitivity. Third, by using an RF pulse that excites all resonances, the CF_2 resonances are J-coupled, which significantly shortens their apparent T_2 (23) and thus the sensitivity; this effect cannot be avoided with the proposed technique. Finally, as demonstrated, in the case of 2D CSE imaging, CSD artifacts from perfluorocarbons just outside the slice should also be taken into account. 3D versions of these techniques that cover a large volume avoid this potential issue, do not come with any SNR penalty, and are thus preferentially to be used. This study was furthermore performed at 3T in light of future clinical applications. However, most ^{19}F MR studies are still performed at higher magnetic field strengths, where the efficacy of the CSE techniques remains to be demonstrated in future studies.

Since techniques similar to the proposed CSE reconstruction algorithm are used for fat-water separation (22,28,29), CSE also has the potential to be applied to separate the signals of two differently distributed fluorinated compounds through iterative optimization. One possible application is the separation of perfluorocarbon signal from that of the anesthetic isoflurane (30), which is commonly used in animal studies and contains two fluorinated groups that may confound image interpretation (31). A GRE implementation was recently demonstrated (32); a bSSFP implementation may be more challenging due to the time-intensive iterative calculations that are also sensitive to perturbations.

In conclusion, we demonstrated the feasibility of a novel ^{19}F MR imaging technique that enables the unambiguous visualization of compounds with complex spectra, and demonstrated its high sensitivity both in vitro and in vivo.

Acknowledgments

We would like to thank Prof. Ulrich Flögel for his kind gift of the perfluorooctyl bromide emulsion, and Prof. Matthias Stuber for insightful discussions. We would also like to thank the Centre d'Imagerie BioMédicale (CIBM) for MR scanning support and infrastructure. This work was furthermore supported by grants from the Swiss Heart Foundation, the Swiss Multiple Sclerosis Society, and the Swiss National Science Foundation (PZ00P3-154719) to RBvH, as well as National Institutes of Health NIDDK Wisconsin Multidisciplinary K12 Urologic Research Career Development Program grant K12DK100022 (PD: D. Bjorling).

References

1. Ruiz-Cabello J, Barnett BP, Bottomley PA, Bulte JW. Fluorine (19F) MRS and MRI in biomedicine. NMR Biomed. 2011; 24(2):114–129. [PubMed: 20842758]
2. Ahrens ET, Zhong J. In vivo MRI cell tracking using perfluorocarbon probes and fluorine-19 detection. NMR Biomed. 2013; 26(7):860–871. [PubMed: 23606473]
3. Temme S, Jacoby C, Ding Z, Bonner F, Borg N, Schrader J, Flogel U. Technical Advance: Monitoring the trafficking of neutrophil granulocytes and monocytes during the course of tissue inflammation by noninvasive 19F MRI. J Leukoc Biol. 2013; 95(4):689–697. [PubMed: 24319285]
4. Srinivas M, Tel J, Schreibelt G, Bonetto F, Cruz LJ, Amiri H, Heerschap A, Figdor CG, de Vries IJ. PLGA-encapsulated perfluorocarbon nanoparticles for simultaneous visualization of distinct cell populations by 19F MRI. Nanomedicine (Lond). 2015; 10(15):2339–2348. [PubMed: 26251876]
5. Ahrens ET, Flores R, Xu H, Morel PA. In vivo imaging platform for tracking immunotherapeutic cells. Nature biotechnology. 2005; 23(8):983–987.
6. Gaudet JM, Ribot EJ, Chen Y, Gilbert KM, Foster PJ. Tracking the fate of stem cell implants with fluorine-19 MRI. PLoS One. 2015; 10(3):e0118544. [PubMed: 25767871]
7. Ribot EJ, Gaudet JM, Chen Y, Gilbert KM, Foster PJ. In vivo MR detection of fluorine-labeled human MSC using the bSSFP sequence. Int J Nanomedicine. 2014; 9:1731–1739. [PubMed: 24748787]
8. Flogel U, Ding Z, Hardung H, Jander S, Reichmann G, Jacoby C, Schubert R, Schrader J. In vivo monitoring of inflammation after cardiac and cerebral ischemia by fluorine magnetic resonance imaging. Circulation. 2008; 118(2):140–148. [PubMed: 18574049]
9. Balducci A, Helfer BM, Ahrens ET, O'Hanlon CF 3rd, Wesa AK. Visualizing arthritic inflammation and therapeutic response by fluorine-19 magnetic resonance imaging (19F MRI). J Inflamm (Lond). 2012; 9(1):24. [PubMed: 22721447]
10. van Heeswijk RB, De Blois J, Kania G, Gonzales C, Blyszczuk P, Stuber M, Eriksson U, Schwitter J. Selective in vivo visualization of immune-cell infiltration in a mouse model of autoimmune myocarditis by fluorine-19 cardiac magnetic resonance. Circ Cardiovasc Imaging. 2013; 6(2):277–284. [PubMed: 23343515]
11. Shin SH, Kadayakkara DK, Bulte JW. In Vivo 19F MR Imaging Cell Tracking of Inflammatory Macrophages and Site-specific Development of Colitis-associated Dysplasia. Radiology. 2017; 282(1):194–201. [PubMed: 27440581]
12. Ahrens ET, Helfer BM, O'Hanlon CF, Schirda C. Clinical cell therapy imaging using a perfluorocarbon tracer and fluorine-19 MRI. Magn Reson Med. 2014; 72(6):1696–1701. [PubMed: 25241945]
13. Riess JG. Oxygen carriers ("blood substitutes")--raison d'etre, chemistry, and some physiology. Chemical reviews. 2001; 101(9):2797–2920. [PubMed: 11749396]
14. Jacoby C, Temme S, Mayenfels F, Benoit N, Krafft MP, Schubert R, Schrader J, Flogel U. Probing different perfluorocarbons for in vivo inflammation imaging by 19F MRI: image reconstruction, biological half-lives and sensitivity. NMR Biomed. 2014; 27(3):261–271. [PubMed: 24353148]

15. van Gorp JS, Seevinck PR, Andreychenko A, Raaijmakers AJ, Luijten PR, Viergever MA, Koopman M, Boer VO, Klomp DW. (19)F MRSI of capecitabine in the liver at 7 T using broadband transmit-receive antennas and dual-band RF pulses. NMR Biomed. 2015; 28(11):1433–1442. [PubMed: 26373355]
16. Lee HK, Nalcioglu O. Reblurred deconvolution method for chemical shift removal in F-19 (PFOB) MR imaging. J Magn Reson Imaging. 1992; 2(1):53–61. [PubMed: 1623281]
17. Meissner M, Reisert M, Hugger T, Hennig J, von Elverfeldt D, Leupold J. Revealing signal from noisy (19) F MR images by chemical shift artifact correction. Magn Reson Med. 2015; 73(6): 2225–2233. [PubMed: 25042821]
18. Giraudeau C, Flament J, Marty B, Boumezbeur F, Meriaux S, Robic C, Port M, Tsapis N, Fattal E, Giacomini E, Lethimonnier F, Le Bihan D, Valette J. A new paradigm for high-sensitivity 19F magnetic resonance imaging of perfluorooctylbromide. Magn Reson Med. 2010; 63(4):1119–1124. [PubMed: 20373415]
19. Goette MJ, Keupp J, Rahmer J, Lanza GM, Wickline SA, Caruthers SD. Balanced UTE-SSFP for 19F MR imaging of complex spectra. Magn Reson Med. 2015; 74(2):537–543. [PubMed: 25163853]
20. Jacoby, C., Oerther, T., Temme, S., Flögel, U. Proc Int Soc Magn Reson Med. Vol. 2927. Toronto, Ontario, Canada: 2014. Simultaneous MR imaging at different resonance frequencies using multi chemical shift selective (MCSS) RARE.
21. Yildirim, M., Keupp, J., Nicolay, K., Lamerichs, R. Proc Int Soc Magn Reson Med. Vol. 3257. Toronto, Ontario, Canada: 2008. Assessment of SNR and detection sensitivity of F-uTSI.
22. Brodsky EK, Holmes JH, Yu H, Reeder SB. Generalized k-space decomposition with chemical shift correction for non-Cartesian water-fat imaging. Magn Reson Med. 2008; 59(5):1151–1164. [PubMed: 18429018]
23. Colotti R, Bastiaansen JAM, Wilson A, Flögel U, Gonzales C, Schwitter J, Stuber M, van Heeswijk RB. Characterization of perfluorocarbon relaxation times and their influence on the optimization of fluorine-19 MRI at 3 Tesla. Magn Reson Med. 2017; 77(6):2263–2271. [PubMed: 27385530]
24. Scheffler K, Lehnhardt S. Principles and applications of balanced SSFP techniques. Eur Radiol. 2003; 13(11):2409–2418. [PubMed: 12928954]
25. Delacoste, J., Chaptinel, J., Beigelman, C., Piccini, D., Sauty, A., Stuber, M. Proc Int Soc Magn Reson Med. Vol. 1455. Toronto, Canada: 2015. A Double Echo Ultra Short Echo Time Acquisition for Respiratory Motion Suppressed High Resolution Imaging of the Lung.
26. Getz GS, Reardon CA. Animal models of atherosclerosis. Arterioscler Thromb Vasc Biol. 2012; 32(5):1104–1115. [PubMed: 22383700]
27. Herrmann KH, Kramer M, Reichenbach JR. Time Efficient 3D Radial UTE Sampling with Fully Automatic Delay Compensation on a Clinical 3T MR Scanner. PLoS One. 2016; 11(3):e0150371. [PubMed: 26975051]
28. Henze Bancroft LC, Strigel RM, Hernando D, Johnson KM, Kelcz F, Kijowski R, Block WF. Utilization of a balanced steady state free precession signal model for improved fat/water decomposition. Magn Reson Med. 2016; 75(3):1269–1277. [PubMed: 25946145]
29. Hernando D, Karampinos DC, King KF, Haldar JP, Majumdar S, Georgiadis JG, Liang ZP. Removal of olefinic fat chemical shift artifact in diffusion MRI. Magn Reson Med. 2011; 65(3): 692–701. [PubMed: 21337402]
30. Constantinides C, Maguire ML, Stork L, Swider E, Srinivas M, Carr CA, Schneider JE. Temporal accumulation and localization of isoflurane in the C57BL/6 mouse and assessment of its potential contamination in 19 F MRI with perfluoro-crown-ether-labeled cardiac progenitor cells at 9.4 Tesla. J Magn Reson Imaging. 2016
31. van Heeswijk RB, Pellegrin M, Flogel U, Gonzales C, Aubert JF, Mazzolai L, Schwitter J, Stuber M. Fluorine MR Imaging of Inflammation in Atherosclerotic Plaque in Vivo. Radiology. 2015; 275(2):421–429. [PubMed: 25496216]
32. Ludwig KD, Hernando D, Roberts NT, van Heeswijk RB, Fain SB. A Chemical Shift Encoding (CSE) Approach for Spectral Selection in Fluorine-19 MRI. Magn Reson Med. 2017 In Press.

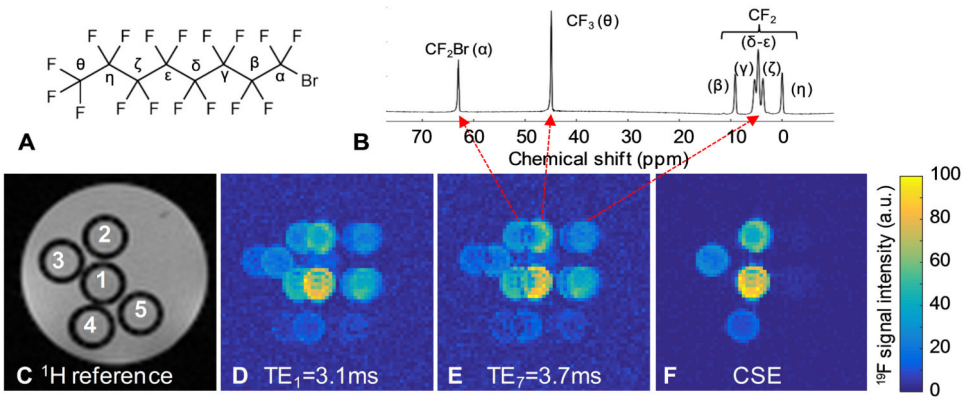

Figure 1. CSE-bSSFP imaging of PFOB

A) The molecular structure of PFOB. **B)** A ^{19}F MR spectrum of PFOB, with three separate resonance structures. **C)** An axial ^{1}H reference image of the phantom with the numbered tubes; tube 5 does not contain PFOB. **D-E)** Direct-FFT ^{19}F images at the shortest and longest TE of the CSE-bSSFP. The CSD artifacts can be directly traced back to the structures of the spectrum (red arrows). Note the negligible signal decrease between the two images. **F)** The CSE-reconstructed image has high SNR and only very faint CSD artifacts (4% of the original intensity).

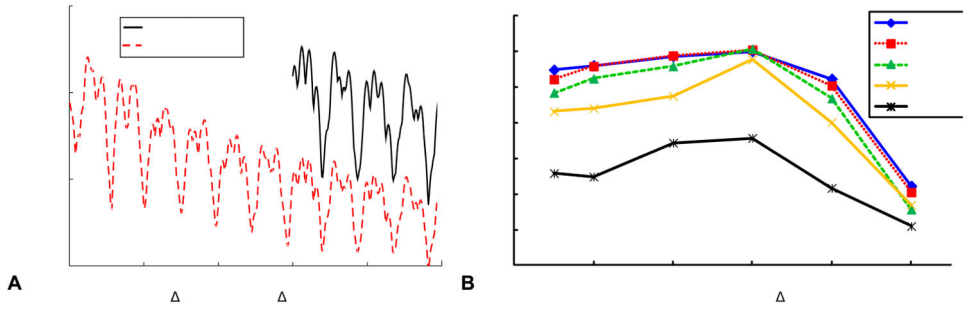

Figure 2. Variation of CSE-bSSFP sensitivity due to parameter choice

A) Bloch equation simulations of the sensitivity as a function of the repetition time for two different sampling bandwidths. As TR increases, the off-resonance signal nulling bands shift, and the contribution of the various resonances changes. While a shorter TR is in general better, certain values see several resonances cancelled out and lead up to 35% sensitivity loss. **B)** Phantom measurements of the influence of the echo time increment ΔTE on the sensitivity. There is relative broad optimum of 0.1-0.4ms, while a trend of lower sensitivity with higher ΔTE (and thus longer TR) can be observed. Note that both graphs have non-zero intercepts; the absolute variation is moderate.

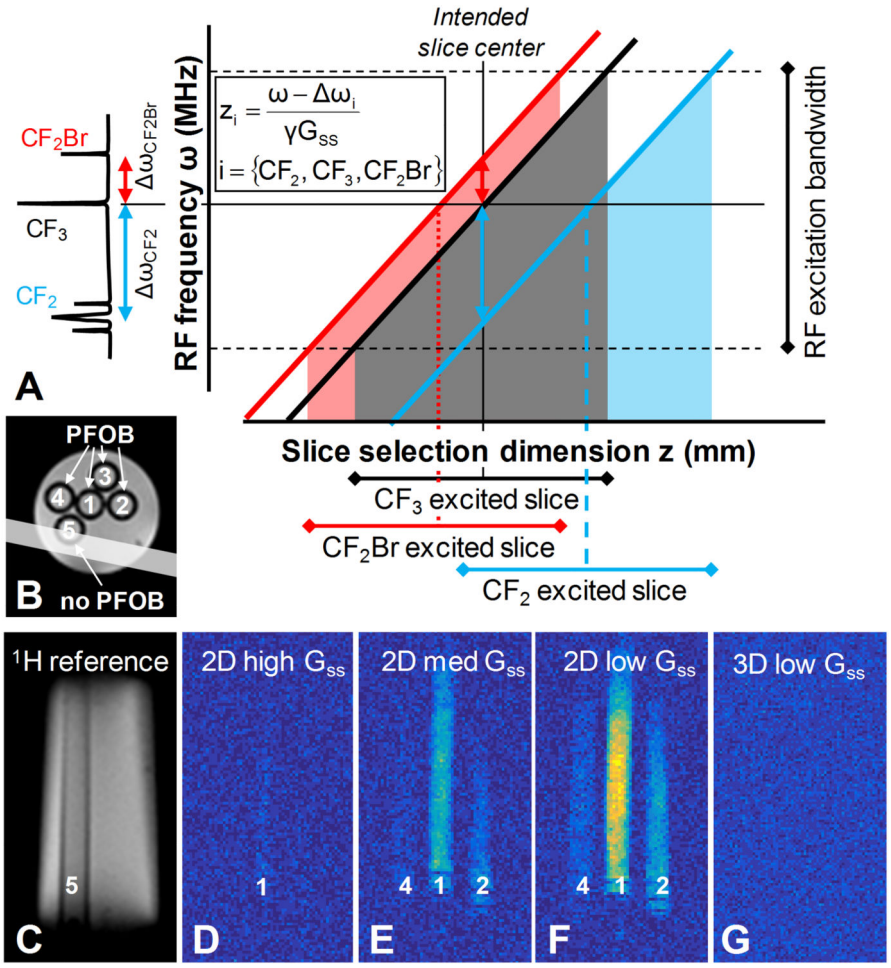

Figure 3. Demonstration of a chemical shift displacement artifact in the slice selection direction

A) Illustration of the different slices that are selected for the three PFOB resonances. An RF pulse with a certain bandwidth (dashed horizontal black lines) is combined with a slice selection gradient G_{ss}, and excites the intended slice (in grey) for the CF_3 resonance. However, the same RF frequencies and gradient correspond to shifted locations for the CF_2 (blue, $\Delta\omega_{CF2}$) and CF_2Br (red, $\Delta\omega_{CF2Br}$) resonances. Note that this is only signal selection and not spatial encoding. **B)** A transverse ^{1}H image through the phantom shows the location of the individual tubes and a 5mm thick slice through tube 5, which contains no PFOB and should thus generate no ^{19}F signal. **C)** The ^{1}H image at this location with tube 5 clearly visible. **D-F)** ^{19}F images at the same location with RF pulses that use different G_{ss}. While the RF pulse profile is the least rectangular for the first image, it sees the least out-of-slice signal being included. The images acquired with the lower G_{ss} see more off-resonance signal included. Also note that no multiple chemical shift ghosts are visible despite the readout direction being left-right, since only a single out-of-slice off-resonance is excited and included in the image. **G)** During a thick-slab 3D acquisition, all resonances are excited and correctly spatially encoded by the phase encoding in the third dimension, resulting in the absence of signal in this slice.

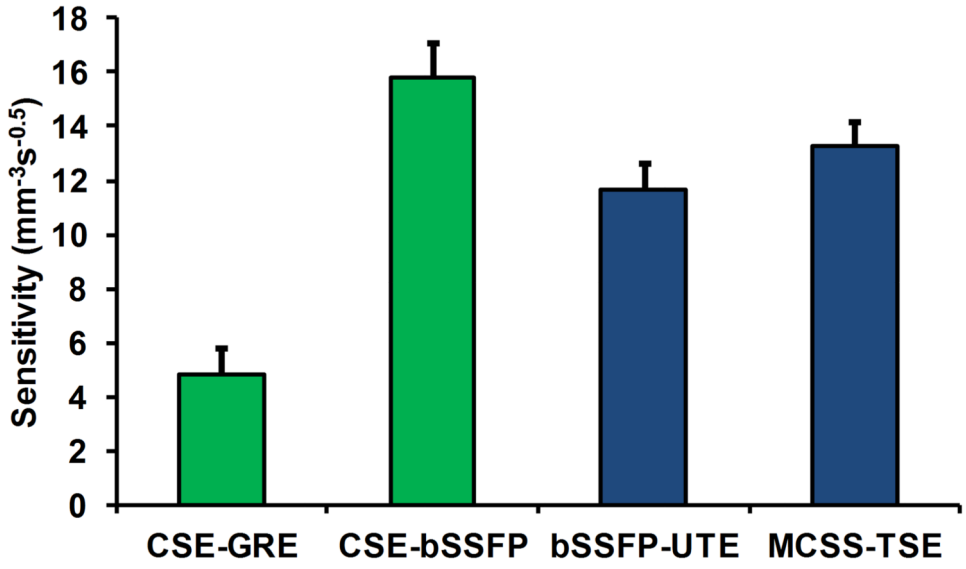

Figure 4. A comparison of the sensitivity of the four pulse sequences in the phantom study

While the CSE-GRE has a low sensitivity, the proposed CSE-bSSFP acquisition has higher sensitivity than the established pulse sequences.

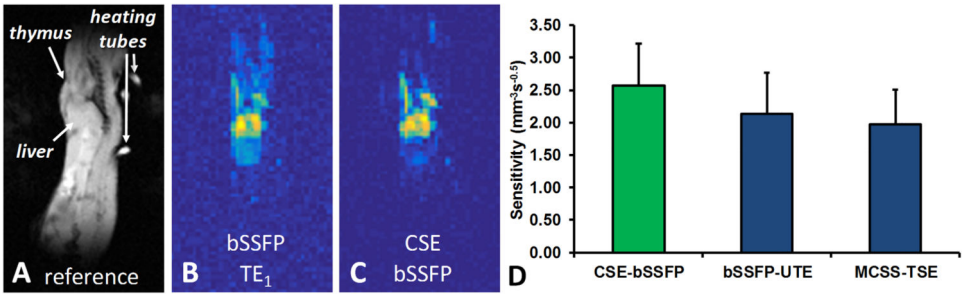

Figure 5. In vivo CSE imaging

A) Sagittal ^{1}H GRE image of the mouse chest and abdomen. **B)** The first echo time image of the ^{19}F CSE-bSSFP series. **C)** ^{19}F CSE reconstructed image. Signal can be observed in the liver, thymus and peritoneal cavity below the liver. **D)** Comparison of the sensitivity of the three applied pulse sequences, which had slightly different strengths relative to one another when compared to the phantom study. Note that the sensitivity is not normalized to the PFOB concentration, and is thus lower than in the phantom study.